

# Comparative *in-silico* study of aqueous humour flow and drug release from intraocular implants for glaucoma treatment

Umar Pitafi<sup>1</sup>, Cynthia Yu-Wai-Man<sup>2</sup>, Tao Chen<sup>1</sup>, Daniel Sebastia-Saez<sup>1</sup>

<sup>1</sup>School of Chemistry and Chemical Engineering, University of Surrey, Guildford, GU2 7XH, UK

<sup>2</sup>Faculty of Life Sciences & Medicine, King's College London, London, SE1 1UL, UK

## Keywords

Computational Fluid Dynamics; glaucoma; intraocular pressure; ocular drug-releasing implant; drug delivery

## Corresponding Authors:

Cynthia Yu-Wai-Man, King's College London, [cynthia.yu-wai-man@kcl.ac.uk](mailto:cynthia.yu-wai-man@kcl.ac.uk)

Daniel Sebastia-Saez, University of Surrey, [j.sebastiasaez@surrey.ac.uk](mailto:j.sebastiasaez@surrey.ac.uk)

## List of symbols

### *Latin symbols*

$c$  – Concentration; mol·m<sup>-3</sup>

$c_{un}$  – Concentration of undissolved species; mol·m<sup>-3</sup>

$D$  – Diffusion coefficient; m<sup>2</sup>·s<sup>-1</sup>

$\vec{g}$  – Acceleration due to gravity; m·s<sup>-2</sup>

$h_C, h_i, h_{il}$  – Height of anterior chamber, iris and iris-lens channel respectively; mm

$I$  – Identity matrix

$\vec{j}$  – Molar flux; mol·m<sup>-2</sup>·s<sup>-1</sup>

$k_b$  – Boltzmann constant; J·K<sup>-1</sup>

$L_{TM}$  – Length of the trabecular meshwork; mm

$MW$  – Molecular weight; Da

$p$  – Pressure; Pa

$r$  – Molecular radius; Å

$R_C, R_L, R_p$  – Radius of posterior cornea, lens and pupil respectively; mm

$T$  – Temperature; K

$\vec{u}$  – Velocity;  $\text{m}\cdot\text{s}^{-1}$

*Greek symbols*

$\beta$  – Dissolution rate;  $\text{m}^2\cdot\text{s}^{-1}\cdot\text{mol}^{-2/3}$

$\varepsilon$  – porosity; dimensionless

$\kappa$  – Permability;

$\mu$  – Dynamic viscosity;  $\text{Pa}\cdot\text{s}$

$\rho$  – Density;  $\text{kg}\cdot\text{m}^{-3}$

*Other symbols*

$\nabla$  – Nabla operator

### **List of abbreviations**

AC – Anterior chamber

AH – Aqueous humour

ALT – Argon laser trabeculoplasty

AS – Anterior segment

CFD – Computational Fluid Dynamics

ECM – Extracellular matrix

FEM – Finite Element Method

IOP – Intraocular Pressure

PC – Posterior chamber

PLGA – poly(lactic-co-glycolic) acid

SLT – Selective laser trabeculoplasty

TM – Trabecular meshwork

## **Abstract**

Drug-releasing implants are gaining momentum in the treatment of glaucoma. Implants present however several limitations. Among these limitations, there is the inability to provide an even distribution of the drug in the trabecular meshwork. CFD simulations were used in this work to study the interplay between ocular fluid dynamics and drug diffusion to explore the options to achieve a homogeneous drug distribution. The analysis finds that thermal convective currents do not result in enough mixing within the eye's anterior chamber. This results in highly localized drug delivery in the trabecular meshwork when using a gravity-driven location cylindrical implant. Locating the implant in the posterior chamber results in improved mixing, although it presents the risk of therapeutical drugs being absorbed by the corneal epithelium. Finally, a ring implant next to the trabecular meshwork is tested, which would give rise to a homogeneous concentration around the entirety of the trabecular meshwork. While implanting a ring next to the trabecular meshwork can entail significant surgical challenges, the solution could consist in cylinders of different length to attain a sufficient evacuation rate of aqueous humour depending on the characteristics of each patient.

## 1. Introduction

Glaucoma is a chronic, progressive optic neuropathy affecting around 70 million people worldwide [1]. This condition is characterised by elevated intraocular pressure (IOP), which results from increased resistance to the outflow of aqueous humour (AH). Glaucoma causes irreversible damage to the optic nerve and ultimately blindness [2]. **Error! Reference source not found.** shows a schematic of the eye's anterior segment. The latter comprises the anterior chamber (AC), i.e., the space between the cornea and the iris, and the posterior chamber (PC). The conventional outflow pathway of the AH is represented by the blue arrow. The AH is produced at the ciliary body at a rate between  $1.5 \mu\text{l}/\text{min}$  and  $3 \mu\text{l}/\text{min}$  [3]. From there, the fluid flows through the gap between the iris and the lens into the anterior chamber (AC) of the eye. It then reaches the trabecular meshwork (TM), where it is absorbed into the systemic circulation through the collector channels of the Schlemm's canal. The conventional outflow pathway is responsible for the evacuation of between 80 and 90% of the AH, with the alternative route being the uveoscleral pathway [4,5], where the AH diffuses through the intercellular spaces of the ciliary body and is responsible for the evacuation of the remaining AH. The uveoscleral pathway has not been considered in this study.

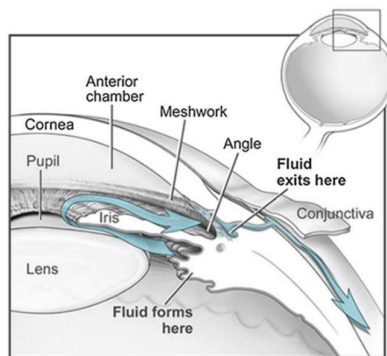


*Figure 1 Schematic illustration of aqueous humour flow within the eye's anterior chamber. Image reproduced with permission from [6]*

Glaucomatous conditions can develop in two ways, including open-angle glaucoma and closed-angle glaucoma. In open-angle glaucoma, the most common type, the TM loses its capacity to evacuate the AH due to fibrosis. The TM consists of an extracellular matrix (ECM), which is formed of collagen, fibronectin, fibrillin and hyaluronic acid and is filled with trabecular cells. Fibrosis, which is the excessive deposition of the ECM components in the TM leads to a reduced evacuation capability of the AH, hence resulting in increased IOP [7]. Under normal physiological conditions, IOP ranges between 10–21 mmHg. The risk of developing glaucoma increases significantly with IOP readings exceeding 21 mmHg. Closed-angle glaucoma is less

common than open-angle glaucoma, and is characterised by an abnormally narrow iridocorneal angle, which results in increased resistance of AH outflow. The simulations included in this study reproduce an open-angle glaucoma scenario.

The most common way to treat glaucoma focus on regulating IOP using topical eye drops that release beta blockers to reduce the production rate of AH and/or outflow resistance [8]. Another common option is laser trabeculoplasty, which includes Selective Laser Trabeculoplasty (SLT) and Argon Laser Trabeculoplasty (ALT). These methods target the tissue of the TM to facilitate drainage. Invasive surgical interventions, like trabeculectomy and tube surgery, may become necessary in severe cases, but can cause side effects, such as cataract formation, hypotony and endophthalmitis [9]. In the case of closed-angle glaucoma, several forms of surgery exist, including laser iridotomy and iridoplasty.

The effectiveness of treatments based on eye drops relies heavily on patients' adherence, which is generally poor [10]. The optimal treatment would provide a sustained drug release over time with zero reliance on patient adherence. Given the limitations of topical treatments and surgery, the use of drug reservoirs, such as punctal plugs and external ocular inserts, is gaining momentum of late [11,12].

To date, Durysta<sup>®</sup> is the only implant approved by the FDA and available commercially [13,14]. Durysta<sup>®</sup> is placed in the lower part of the iridocorneal angle, at the entry to the TM. With its standard cylindrical dimensions (i.e. diameter 0.2 mm and 1 mm length), one of the concerns with the use of Durysta<sup>®</sup> is the difficulty to achieve a homogeneous concentration of the released drug across the TM. While the placement of Durysta<sup>®</sup> in the AC is driven by gravity, there are other placement solutions being developed. For instance, the travoprost implant iDose<sup>®</sup> TR uses a trabecular anchor [15,16]. Further, another method under clinical trial at present is based on attaching a ring-shaped drug reservoir on the haptic legs of intraocular lenses (IOL) used in cataract surgery (<https://www.spyglasspharma.com>)

Understanding the interplay between ocular fluid dynamics and mass transport is key to accelerate the development of effective IOP-reducing drug-releasing ocular implants. Mathematical simulations (i.e., *in-silico* methods) are gaining momentum as some authors highlight the small size of the AC and the implant as a limitation to carry out their experimental studies [17], among other difficulties, including ethical issues. Further, *in-silico* methods can contribute to test different implant-location and size scenarios swiftly, hence suggesting further ways of drug delivery improvement.

There is a growing number of studies that deal with simulations of drug diffusion within the eye using Computational Fluid Dynamics (CFD) [18]. Specifically, the flow of the aqueous humour has been analysed in some studies. An example of the aqueous humour flow description can be seen in [19], where the authors simulate the flow of AH in the collector channels of the Schlemm’s canal. A recent example of drug diffusion simulation is the work reported in [20], where administration of timolol using therapeutic contact lenses was simulated. Recent work from [21] describes a detailed simulation of a drug-releasing, ring-shaped implant mounted on the haptic legs of an IOL. The authors simulate how the release of the drug reduces the resistance to the AH flow in the TM, which is described as a porous medium using Darcy’s law.

In this work, a CFD methodology that includes laminar flow, heat transfer, mass transport and drug release kinetics is employed to compare the 3-dimensional spatio-temporal evolution of the bimatoprost concentration released by a cylindrical porous implant mimicking Durysta<sup>®</sup>—placed in the AC, where the concentration is proven to be highly localised—and the same implant located in the PC, mimicking the shape and dimensions of Durysta<sup>®</sup> but placed near the lens as the solution presented by SpyGlass Pharma<sup>™</sup>.

## 2. Methodology

The simulations were carried out using the commercial FEM software COMSOL Multiphysics v6.3. The model represents a 3-D geometry of the human eye’s anterior segment (AS) to analyze AH flow, heat transfer and drug release and transport from the porous intraocular implant. The geometric parameters are summarized in Table 1 while Figure 2 shows a schematic of the computational domain with mesh detail.

*Table 1 Geometry parameters of the anterior segment.*

<b>Parameter</b>	<b>Value [mm]</b>
Radius of posterior cornea [6]	6.80
Maximum height of anterior segment [6]	2.63
Lens radius [6]	10.00
Height of iris-lens channel [6,22,23]	0.093
Iris thickness [24]	0.40
Pupil radius [23]	1.75

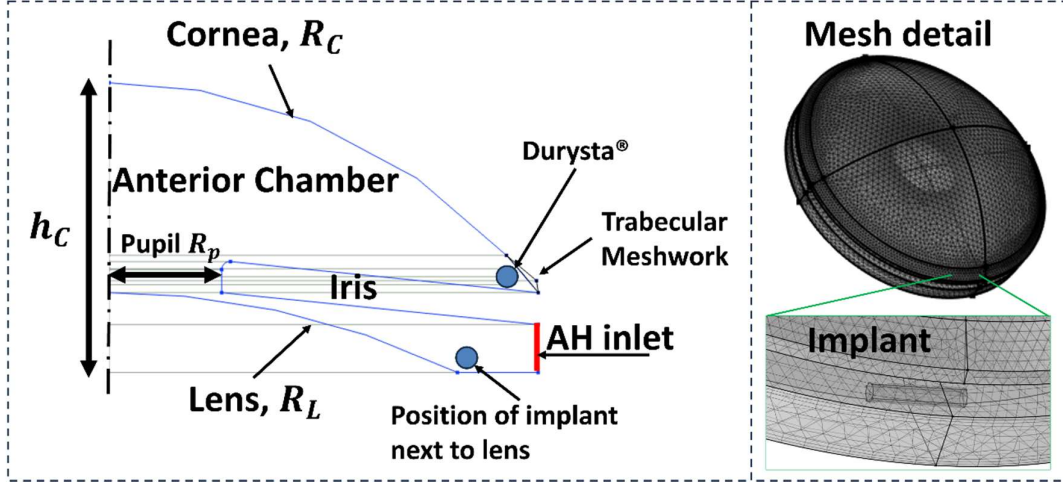


Figure 2 Schematic of the calculation domain. The geometry of the anterior segment was reproduced in 2-D and revolved around the symmetry axis, after which, a cylinder mimicking the implant was included.

The implant was represented as a cylindrical porous medium with a diameter of 0.2mm and a length of 1mm placed in either (i) at the iridocorneal angle or (ii) at the vicinity of the IOL in the posterior chamber. This allowed a comparison of concentration profiles depending on implant location.

## 2.1 Fluid Dynamics

AH flow was modelled as an incompressible, Newtonian single phase laminar flow during the first (static) step of the simulation. The flow field was computed using the laminar flow physics interface in COMSOL Multiphysics v6.3, solving the steady state Navier-Stokes equations. The conservation of momentum equation is:

$$\rho(\mathbf{u} \cdot \nabla)\mathbf{u} = \nabla \cdot [-p\mathbf{I} + \mathbf{K}] + \mathbf{F} + \rho\mathbf{g} \quad (1)$$

And the conservation of mass:

$$\rho\nabla \cdot \mathbf{u} = 0 \quad (2)$$

Where  $\rho$  represents the density,  $\mathbf{u}$  is the velocity vector,  $\mathbf{K}$  represents the viscosity forces acting on the fluid,  $p$  is the pressure,  $\mathbf{I}$  is the identity matrix, and  $\mathbf{g}$  is the acceleration due to gravity.  $\mathbf{F}$  is the thermally driven buoyant force which can be defined using the Boussinesq approximation. The trabecular meshwork and the implant were represented as porous subdomains, where the local momentum balance was modified according to Darcys law. The implant was assigned a porosity of 0.9 (i.e., PLGA scaffold) [25]. The geometric and flow parameters of the trabecular meshwork were obtained from [26].

A no-slip boundary condition was implemented in the cornea, lens, iris, and haptic legs of the implant. An outlet boundary condition was set on the TM. A uniform inflow velocity of  $v_0 = 2.03 \mu\text{m}\cdot\text{s}^{-1}$  was imposed at the AH inlet, corresponding to a physiological AH production rate of approximately  $2.5 \mu\text{l}/\text{min}$  [27]. A static intraocular pressure of 27 mmHg was applied to represent glaucomatous conditions [6]. Gravitational acceleration was included to assess the effect of body orientation (i.e., standing or supine) on AH flow.

## 2.2 Heat Transfer

The effect of heat transfer on AH flow was also calculated in the first step (static) of the simulations. To capture the thermally driven convective flow of AH. The heat transfer formulation employed in this study can be directly related to Pennes' Bioheat equation which in its general form is expressed as:

$$\rho c_p \frac{\partial T}{\partial t} = \nabla \cdot (k \nabla T) + \rho_b c_b \omega_b (T_a - T) + Q_{met} + Q_{ext} \quad (3)$$

Where the additional terms  $\rho_b c_b \omega_b (T_a - T)$  and  $Q_{met}$  account for blood perfusion and metabolic heat generation within biological tissues. In the case of AH, these effects are negligible because the fluid is avascular and has no metabolic activity. Furthermore the simulations were conducted under steady state conditions allowing the transient term  $\frac{\partial T}{\partial t}$  to be omitted. The symbols  $\rho$ ,  $c_p$  and  $k$  are the density, specific heat capacity and thermal conductivity of AH respectively.

Imposed boundary conditions were defined following the methodology in [28]. At the corneal surface heat loss to the surrounding environment was modelled as a combination of convective, radiative and evaporative effects expressed as

$$-n \cdot q = q_{conv} + q_{rad} + q_{evap} \quad (4)$$

Where  $n$  is the unit outward normal vector and  $q$  is the conductive heat flux vectors. The individual fluxes were specified as separate boundary conditions in COMSOL Multiphysics v6.3 as

$$q_{conv} = h_{amb}(T_{ext} - T) \quad (5)$$

And

$$q_{rad} = \epsilon \sigma (T_{ext}^4 - T^4) \quad (6)$$

Where  $h_{amb}$  is the ambient convective heat transfer coefficient,  $T_{ext}$  and  $T_{amb}$  are external and ambient air temperatures,  $e$  is corneal emissivity and  $\sigma$  is the Stefan Boltzmann constant. A constant evaporative heat flux at the corneal surface,  $q_{evap}$  was assigned a constant value of 40 W/m<sup>2</sup> to average heat loss due to tear-film evaporation under physiological conditions. A summary of parameters is included in Table 2.

Table 2 Numerical values of the parameters used in the eye's thermal boundary conditions.

Parameter	Description	Value
$q_{evap}$	Evaporation rate W m <sup>-2</sup>	40
$\sigma$	Stefan Boltzmann constant W m <sup>-2</sup> K <sup>-4</sup>	5.67e-8
$\varepsilon$	Emissivity	0.975
$h_{bl}$	Blood convection coefficient W m <sup>-2</sup> K <sup>-1</sup>	65
$h_{amb}$	Ambient convection coefficient W m <sup>-2</sup> K <sup>-1</sup>	10
$T_{ext}$	External Temperature K	298
$T_{bl}$	Blood Temperature K	310

### 3.3. Mass transport

The steady-state thermal convective flow calculated in the first step of the simulation was used as the initial conditions to solve the transient transport equation in the second step of the simulations:

$$\frac{\partial c}{\partial t} + \nabla \cdot \mathbf{J} + \mathbf{u} \cdot \nabla c = R \quad (7)$$

Where  $c$  is the concentration of the drug and  $\mathbf{J} = -D\nabla c$  accounts for Fick's diffusion flux. The source term  $R$  accounts in this case for the delivery of the drug from the implant and into the bulk fluid flow of AH. The diffusion coefficient in water was calculated using the well-known Stokes-Einstein equation:

$$D = \frac{k_b T}{6\pi\mu r} \quad (8)$$

Where  $T = 34.51^\circ\text{C}$  is the temperature of the eye and  $\mu = 0.7269 \text{ mPa}\cdot\text{s}$  is the dynamic viscosity of water at that temperature. The parameter  $k_b = 1.380649 \times 10^{-23} \text{ J/K}$  is the Boltzmann constant. The molecular radius  $r$  was calculated using the empirical expression:

$$r = \sqrt[3]{\frac{3}{4\pi} \times 0.9087 \times MW} \quad (9)$$

Which assumes spherical symmetry of the bimatoprost molecule.

Bimatoprost presents a low solubility in the AH, therefore, it is not readily available in the implant for dissolution. Instead, a hydrolysis process takes place before the drug could be carried away by the AH flow. Delivery from the implant has thus been implemented using the following equation, also solved during the second (transient) step of the simulation:

$$\frac{\partial c_{un}}{\partial t} = -\beta c_{un} \quad (10)$$

Where  $c_{un}$  is the concentration of undissolved drug in the implant and  $\beta$  is the delivery rate.

### 3. Results and discussion

#### 3.1. Model verification and validation

Validation of CFD eye models presents inherent challenges that have been highlighted in the literature [18]. Validation is thus limited here to the comparison between AH flow patterns obtained with this model and others reported previously in the literature, as well as the value of the AH velocity in the iris-lens gap. Figure 3 and Figure 4 report the comparison of AH flow patterns for the standing and the supine body positions respectively.

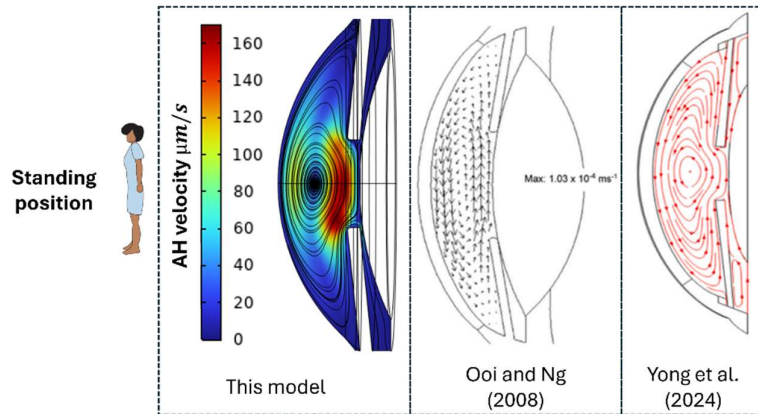


Figure 3 Comparison between the fluid flow patterns obtained with this model and those reported by Ooi et al. [28] and Yong et al. [29] for the standing position.

Differences depending on body position are observed. A central eddy in front of the pupil was observed in standing position and a symmetric arrangement of two eddies formed in a cross-section of the AC in the supine position. Larger values of the AH velocity were observed in standing position close to the pupil. AH maximum velocity was  $150 \mu\text{m/s}$  in the standing

position, which compared well with the values reported in the literature, while a maximum velocity of  $40 \mu\text{m/s}$  was obtained in the supine position.

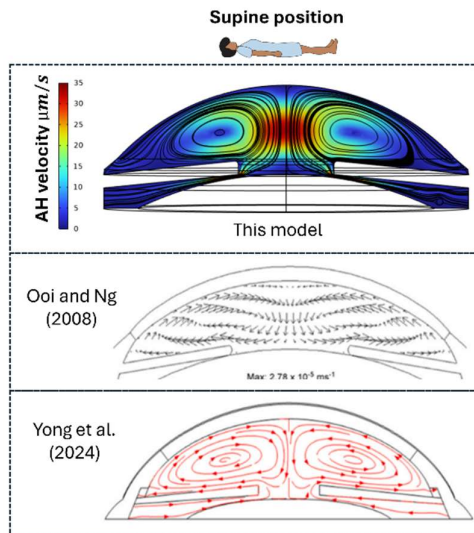


Figure 4 Comparison between the fluid flow patterns obtained with this model and those reported by Ooi et al. [28] and Yong et al. [29] for the standing position.

Verification of the model was performed by checking grid independence using the *fine*, *finer* and *extremely fine* settings, with differences in the results of less than 2% with respect to the *fine* mesh.

### 3.2. Calibration of drug releasing rate from implant ( $\beta$ ).

Calibration of the drug release rate  $\beta$  was performed due to lack of available experimental data. Figure 5 shows the temporal evolution of the amount of drug remaining in the implant during the simulated 12 weeks' delivery for different hypothetical values of  $\beta$ .

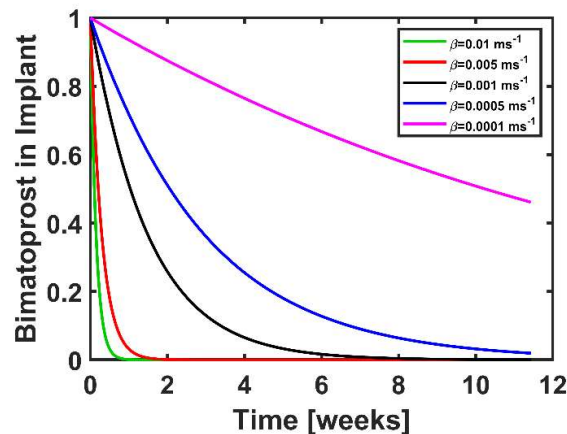


Figure 5 Time-evolution of the implant dose in the standing position. The results were normalised by the initial dose of  $10 \mu\text{g}$ .

The parameter  $\beta$  was calibrated to attain a zero dose after the simulated 12 weeks. Such calibration yields an approximate value between  $\beta = 0.0001\text{--}0.0005\text{ ms}^{-1}$  that has been used to obtain the results reported in subsequent sections.

### 3.3. The effect of implant location on drug delivery

Figure 6 and Figure 7 show bimatoprost concentration maps in the AC for standing and supine body positions respectively. Two locations of the cylindrical implant were evaluated, including the iridocorneal angle (i.e. gravity-driven positioning) and the lower part of the lens in the PC. The results suggest that bimatoprost tends to concentrate in the lower part of the TM when the implant positioning is gravity-driven in the AC. The results suggest then that thermal convection is not an effective mixing mechanism within the AC. This can be seen clearly in the snapshots corresponding to delivery times  $t = 3$  hours, 1 week and 6 weeks. The concentration maps suggest that positioning the implant in next to the lens produces accumulation of the drug in the PC in the standing body position, while the accumulation is restricted to the right-hand side of the AC in the supine position ( $0.2\text{ }\mu\text{g/mL}$  in the AC after 3 hours' delivery time). It is observed too, that in this case, thermal convection eddies act as a mixing mechanism with limited effectivity. It is concluded that positioning the implant next to the lens gives rise to smaller concentrations of the drug over a greater zone within the AC than positioning the implant in the iridocorneal angle. Distributing the drug over a greater volume within the AC can help with avoiding an excessively localised delivery, although it can also carry the effects of reducing the drug's bioavailability and inflammation when bimatoprost permeates the cornea [30].

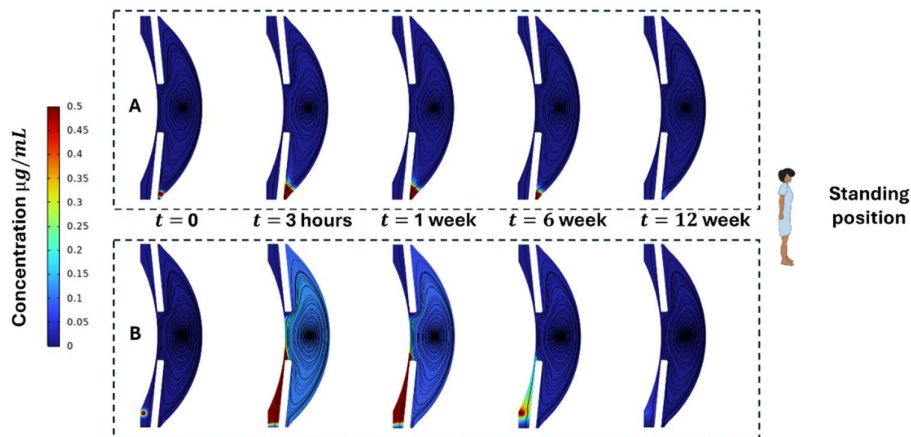


Figure 6 Cross-section colour maps of the bimatoprost concentration [ $\mu\text{g/mL}$ ] in the eye's anterior segment in standing position at different times during the simulated 3 months' delivery. Series (A) shows the results for an implant located in the iridocorneal angle. Series (B) corresponds to the results obtained for a cylindrical implant located in the posterior chamber, next to the lens.

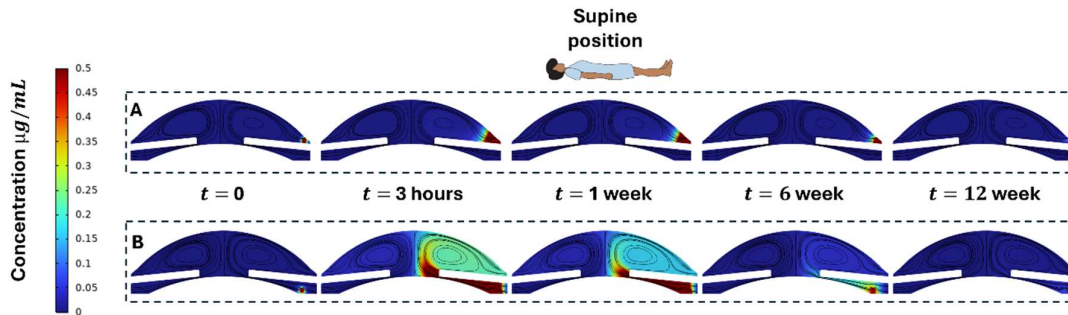


Figure 7 Cross-section maps of the bimatoprost concentration [ $\mu\text{g/mL}$ ] in the eye's anterior segment in supine position at different times during the simulated 3 months' delivery. Series (A) shows the results for the implant placed in the iridocorneal angle. Series (B) corresponds to the results obtained for a cylindrical implant located in the posterior chamber, in the vicinity of the lens.

Figure 8 shows 3-D contour plots of bimatoprost, which provide an idea of the extent of drug distribution in the AC after 1 week's delivery time. Plots have been included for both standing and supine body position and the two implant locations. It is observed that body posture does not affect the extent of drug delivery when the implant is located by gravity in the iridocorneal angle. When the implant is located next to the lens, a distribution over a greater zone is observed in the standing than in the supine position.

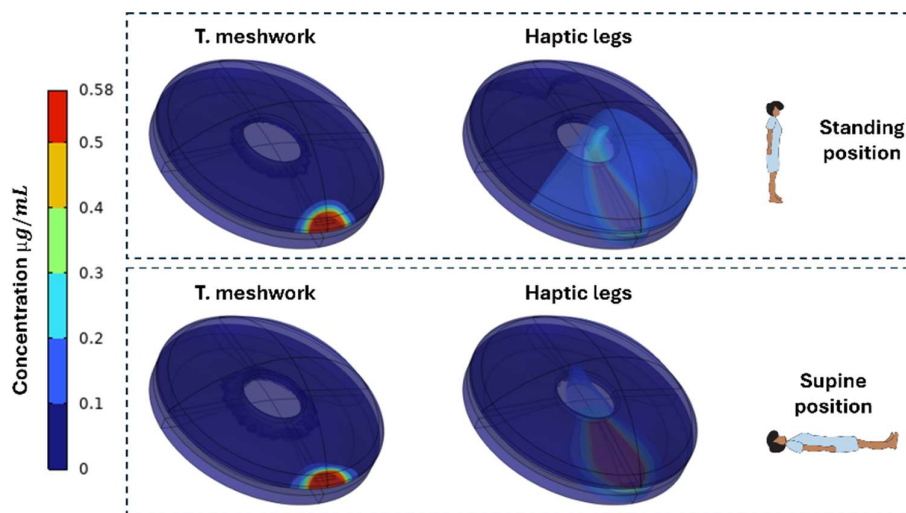


Figure 8 Contour plots of bimatoprost concentration.

The concentration profiles observed may open the door towards discussing which would be the optimal therapeutic strategy for a given patient. Location of the implant in the iridocorneal angle gives way to highly localised drug delivery regardless of body position. It can be speculated that this strategy will be efficient when the effect of the drug in a small portion of the TM is enough to open a way for sufficient AH evacuation. Placing the implant next to the lens gives smaller concentrations but reaches a greater portion of the TM with respect to

iridocorneal positioning. In the latter strategy, there is also a risk that bimatoprost permeates into the corneal epithelium, causing a reduction of the drug's bioavailability and potential inflammation.

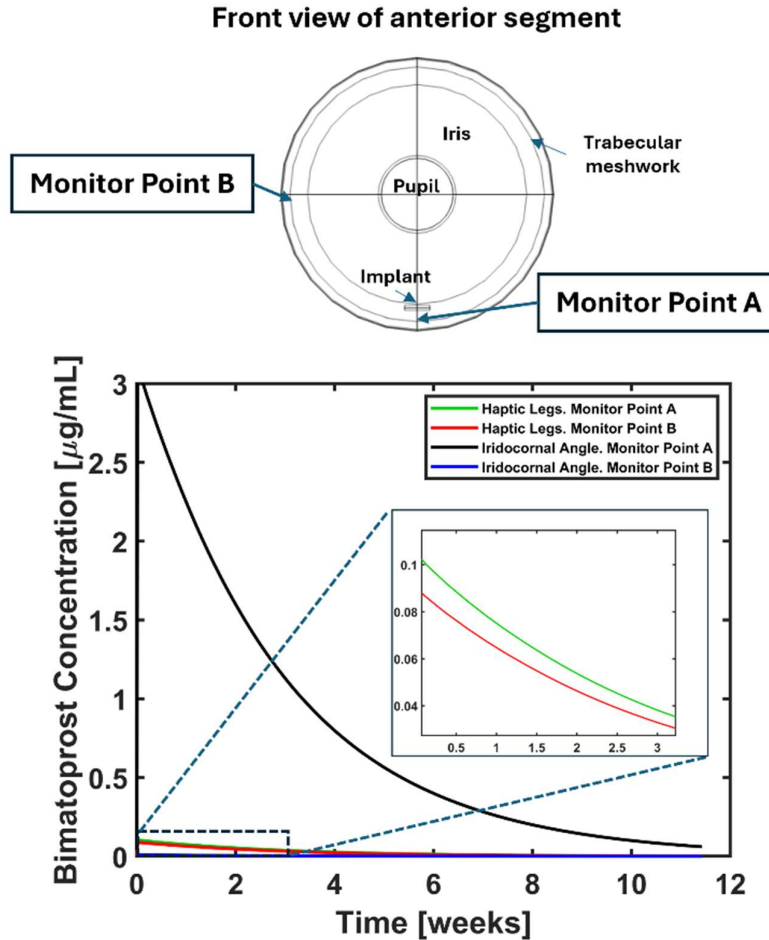


Figure 9 Evolution of drug concentration in the TM during the 12 weeks' delivery.

Figure 9 quantifies drug delivery localisation for the standing position. Two monitor points were set up in the simulations: Monitor Point A corresponds to the boundary between the TM at the lowest part of the eye (i.e., at '6 hours' position), while Monitor Point B corresponds to the side of the eye (i.e., '3 hours' position). When the cylindrical implant is placed in the TM, the concentration in the instant following the beginning of delivery is  $3 \mu\text{g/mL}$  and reduces following the expected exponential trend over the 12 weeks' delivery time, while the concentration observed at '9 hours' position is negligible. When the cylindrical implant is placed next to lens, differences in concentration are smaller, with a value of  $0.1 \mu\text{g/mL}$  in Monitor Point A and  $0.09 \mu\text{g/mL}$  in Monitor Point B.

The results suggest that an annular implant could give way to localised drug delivery in the TM, with only small concentrations reaching the cornea. The results obtained for the hypothetical annular implant are in Figure 10. The same dose of 10  $\mu\text{g}$  has been implemented. The results show a temporal evolution in Monitor Point B of approximately 0.15  $\mu\text{g}/\text{mL}$ . Low concentrations in the TM could be improved by increasing dosage. A 360° annular implant could however entail practical implantation hurdles from the surgical standpoint due to geometric restrictions. The extent of the TM covered by the ring (or the cylindrical arch) would be determined by the AH evacuation needs of each specific patient, hence opening the door towards personalised treatment.

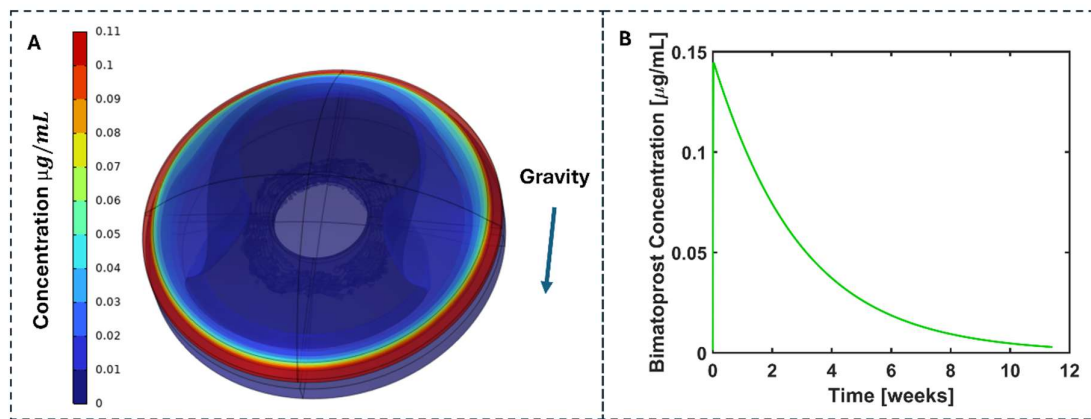


Figure 10 Concentration profiles in the AS for an annular implant (A) and evolution of the concentration at Monitor Point B during delivery time (B).

#### 4. Conclusions

An *in-silico* model of drug-releasing implants in the anterior chamber of the eye is presented in this work. The results suggest that there is a precise balance between convection and diffusion that results in drug release being highly localised on a small portion of the TM when the implant is placed at the iridocorneal angle. The model also suggests that thermal convective currents does not result in efficient mixing to produce homogeneous drug concentrations in the trabecular meshwork. This leaves the dimensions and location of the implant as the available strategies to deliver a homogeneous concentration distribution over the TM. Regarding the location of the implant within the eye, our results suggest that placing the implant next to the lens gives rise to improved homogeneity. An annular implant around the trabecular tested was finally tested, which showed homogeneous bimatoprost concentrations. An annular implant however could entail implementation challenges. An effective solution could be to limit the

arch of the annular implant, in such a way that enough evacuation rate of the aqueous humour is attained for each specific patient's necessities.

## **Funding**

This work is supported by the Medical Research Council (grant number MR/T027932/1).

## **REFERENCES**

1. Faiq MA, Sidhu T, Sofi RA, Singh HN, Qadri R, Dada R, et al. A novel mathematical model of glaucoma pathogenesis. *J Curr Glaucoma Pract.* 2019;13: 3–8. doi:10.5005/jp-journals-10078-1241
2. Killer HE, Pircher A. What is the optimal glaucoma treatment: reducing aqueous humour production or facilitating its outflow? *Eye (Basingstoke).* Springer Nature; 2020. pp. 1719–1721. doi:10.1038/s41433-020-0862-8
3. Goel M, Picciani RG, Lee RK, Bhattacharya SK. Aqueous Humor Dynamics: A Review. *Open Ophthalmol J.* 2010.
4. Weinreb RN, Aung T, Medeiros FA. The pathophysiology and treatment of glaucoma: A review. *JAMA.* American Medical Association; 2014. pp. 1901–1911. doi:10.1001/jama.2014.3192
5. Johnson M, McLaren JW, Overby DR. Unconventional aqueous humor outflow: A review. *Experimental Eye Research.* Academic Press; 2017. pp. 94–111. doi:10.1016/j.exer.2016.01.017
6. Wang W, Qian X, Song H, Zhang M, Liu Z. Fluid and structure coupling analysis of the interaction between aqueous humor and iris. *Biomed Eng Online.* 2016;15. doi:10.1186/s12938-016-0261-3
7. Qin M, Yu-Wai-Man C. Glaucoma: Novel antifibrotic therapeutics for the trabecular meshwork. *European Journal of Pharmacology.* Elsevier B.V.; 2023. doi:10.1016/j.ejphar.2023.175882
8. Conlon R, Saheb H, Ahmed IIK. Glaucoma treatment trends: a review. *Canadian Journal of Ophthalmology.* Elsevier B.V.; 2017. pp. 114–124. doi:10.1016/j.jcjo.2016.07.013
9. Cursiefen C, Cordeiro F, Cunha-Vaz J, Wheeler-Schilling T, Scholl HPN. Unmet Needs in Ophthalmology: A European Vision Institute-Consensus Roadmap 2019–2025. *Ophthalmic Research.* S. Karger AG; 2019. pp. 123–133. doi:10.1159/000501374
10. Walters TR, Lee SS, Goodkin ML, Whitcup SM, Robinson MR. Bimatoprost Sustained-Release Implants for Glaucoma Therapy: 6-Month Results From a Phase I/II Clinical Trial. *Am J Ophthalmol.* 2017;175: 137–147. doi:10.1016/j.ajo.2016.11.020
11. Kesav NP, Capitena Young CE, Ertel MK, Seibold LK, Kahook MY. Sustained-release drug delivery systems for the treatment of glaucoma. *International Journal of Ophthalmology.* International Journal of Ophthalmology (c/o Editorial Office); 2021. pp. 148–159. doi:10.18240/ijo.2021.01.21

12. Ozdemir S, Wong TT, Allingham RR, Finkelstein EA. Predicted patient demand for a new delivery system for glaucoma medicine. *Medicine (United States)*. 2017;96. doi:10.1097/MD.0000000000006626
13. Bacharach J, Tatham A, Ferguson G, Belalcázar S, Thieme H, Goodkin ML, et al. Phase 3, Randomized, 20-Month Study of the Efficacy and Safety of Bimatoprost Implant in Patients with Open-Angle Glaucoma and Ocular Hypertension (ARTEMIS 2). *Drugs*. 2021;81: 2017–2033. doi:10.1007/s40265-021-01624-9
14. Medeiros FA, Walters TR, Kolko M, Coote M, Bejanian M, Goodkin ML, et al. Phase 3, Randomized, 20-Month Study of Bimatoprost Implant in Open-Angle Glaucoma and Ocular Hypertension (ARTEMIS 1). *Ophthalmology*. 2020;127: 1627–1641. doi:10.1016/j.ophtha.2020.06.018
15. Sarkisian SR, Ang RE, Lee AM, Berdahl JP, Heersink SB, Burden JH, et al. Travoprost Intracameral Implant for Open-Angle Glaucoma or Ocular Hypertension: 12-Month Results of a Randomized, Double-Masked Trial. *Ophthalmol Ther*. 2024;13: 995–1014. doi:10.1007/s40123-024-00898-y
16. Bacharach J, Doan L V., Stephens KG, Usner DW, Kothe AC, Katz LJ, et al. Travoprost Intracameral Implant Demonstrates Superior IOP Lowering Versus Topical Prostaglandin Analog Monotherapy in Patients with Open-Angle Glaucoma or Ocular Hypertension. *Ophthalmol Ther*. 2024. doi:10.1007/s40123-024-00992-1
17. Weinreb RN, Christie WC, Medeiros FA, Craven ER, Kim K, Nguyen A, et al. Single Administration of Bimatoprost Implant: Effects on 24-Hour Intraocular Pressure and 1-Year Outcomes. *Ophthalmol Glaucoma*. 2023;6: 599–608. doi:10.1016/j.ogla.2023.06.007
18. Sebastia-Saez D, Luo J, Qin M, Chen T, Yu-Wai-Man C. Advancing glaucoma research with multiphysics continuum mechanics modelling: Opportunities and open challenges. *Journal of the Mechanical Behavior of Biomedical Materials*. Elsevier Ltd; 2026. doi:10.1016/j.jmbbm.2025.107240
19. Martínez Sánchez GJ, Escobar del Pozo C, Rocha Medina JA, Naude J, Brambila Solorzano A. Numerical simulation of the aqueous humor flow in the eye drainage system; a healthy and pathological condition comparison. *Med Eng Phys*. 2020;83: 82–92. doi:10.1016/j.medengphy.2020.07.010
20. Yi H, Feng Y, Gappa-Fahlenkamp H. Analysis of topical dosing and administration effects on ocular drug delivery in a human eyeball model using computational fluid dynamics. *Comput Biol Med*. 2022;141. doi:10.1016/j.compbimed.2021.105016
21. Pandey PK, Jain M, Jha PK. Drug Delivery from a Ring Implant Attached to Intraocular Lens: An in-silico Investigation. *J Pharm Sci*. 2024. doi:10.1016/j.xphs.2024.09.001
22. Ferreira JA, De Oliveira P, Da Silva PM, Murta JN. Numerical simulation of aqueous humor flow: From healthy to pathologic situations. *Appl Math Comput*. 2014;226: 777–792. doi:10.1016/j.amc.2013.10.070
23. Fernández-Vigo JI, Marcos AC, Agujetas R, Montanero JM, Sánchez-Guillén I, García-Feijóo J, et al. Computational simulation of aqueous humour dynamics in the presence

- of a posterior-chamber versus iris-fixed phakic intraocular lens. *PLoS One*. 2018;13. doi:10.1371/journal.pone.0202128
24. Cui L, Xiao Y, Xiang Z, Chen Z, Yang C, Zou H. Study on the correlation between iris blood flow, iris thickness and pupil diameter in the resting state and after pharmacological mydriasis in patients with diabetes mellitus. *BMC Ophthalmol*. 2024;24. doi:10.1186/s12886-024-03322-y
  25. Pan Z, Ding J. Poly(lactide-co-glycolide) porous scaffolds for tissue engineering and regenerative medicine. *Interface Focus*. Royal Society; 2012. pp. 366–377. doi:10.1098/rsfs.2011.0123
  26. Abu-Hassan DW, Acott TS, Kelley MJ. The Trabecular Meshwork: A Basic Review of Form and Function.
  27. Cai JC, Chen YL, Cao YH, Babenko A, Chen X. Numerical study of aqueous humor flow and iris deformation with pupillary block and the efficacy of laser peripheral iridotomy. *Clinical Biomechanics*. 2022;92. doi:10.1016/j.clinbiomech.2022.105579
  28. Ooi EH, Ng EYK. Simulation of aqueous humor hydrodynamics in human eye heat transfer. *Comput Biol Med*. 2008;38: 252–262. doi:10.1016/j.combiomed.2007.10.007
  29. Yong HN, Ismail Z, Lim YJ, Muna'aim MA. Modelling gravity-driven aqueous humour flow and drug delivery in Descemet's membrane detachment. *Alexandria Engineering Journal*. 2024;107: 184–197. doi:10.1016/j.aej.2024.07.019
  30. Chen W, Dong N, Huang C, Zhang Z, Hu J, Xie H, et al. Corneal alterations induced by topical application of commercial latanoprost, travoprost and bimatoprost in rabbit. *PLoS One*. 2014;9. doi:10.1371/journal.pone.0089205